Journal of
Materials Chemistry A

ROYAL SOCIETY
OF CHEMISTRY

PAPER

View Article Online
View Journal | View Issue

Check for updates

Cite this: *J. Mater. Chem. A*, 2025, **13**, 23113

Ti–Cu alloy-based converted suboxides: robust electrode scaffolds for enhanced electrocatalytic glycerol oxidation†

Ula Suliman, Jing Liu* and Shiva Mohajernia*

Received 6th January 2025
Accepted 3rd June 2025

DOI: 10.1039/d5ta00107b

rsc.li/materials-a

Titanium dioxide (TiO_2) nanotubes exhibit high surface area, chemical stability and geometrically favorable electronic properties, posing as a suitable support material for embedded nano-catalysts. However, being semiconductive in nature, TiO_2 nanotubes suffer from limited conductivity. This hampers their use as electrodes especially in anodic applications where they experience significant current blockage. In this study, we investigate the intrinsic decoration of TiO_2 nanotubes with Cu sites and the subsequent defect engineering of the electrodes for enhanced glycerol oxidation. Despite its good electrocatalytic glycerol oxidation performance, Cu suffers from low stability, requiring a sturdy scaffold as a support material. Ti–Cu alloy foils containing trace concentrations of copper were anodized, simultaneously decorating titania nanotubes with Cu species as they grow on the metal substrate, followed by treating the metal–metal oxide electrodes in an optimized reducing environment. Cu nanoparticles as small as 2–3 nm in diameter are formed as a result as well as point defects in the titania lattice such as Ti^{3+} and oxygen vacancies. The presented methodology results in significantly uplifting the conductivity of TiO_2, robustly securing Cu-based catalytic sites on the titania tube walls and allowing for the synergistic interactions between Cu sites and point defects in the titania lattice. These physicochemical changes were confirmed by electron microscopy techniques (FESEM, TEM, HAADF) and surface characterization (XPS, EDX), revealing homogeneously distributed Cu nanoparticles, lattice distortion, and increased Ti^{3+}/Ti^{4+} ratios. The substoichiometric TiO_2 nanotubes also demonstrated an increased capacity to scaffold co-catalysts; this was exemplified using Co deposition, which showed uniform nucleation and stable anchoring, indicative of improved chemical compatibility and interface engineering. Electrochemical analysis demonstrated a significant improvement in activity, where binder-free Cu-decorated electrodes treated in a hydrogen environment at 500 °C showed up to 239 times higher glycerol oxidation activity than air-annealed CuTNA, and up to 325 times higher activity than pristine TNAs. The enhancement is attributed to the combination of improved charge transport, increased active surface area, and catalytic synergy between Cu and TiO_2 defect sites. Furthermore, the modified electrodes exhibited Faradaic efficiency as high as 33.69% toward the partial oxidation of glycerol, suggesting favorable selectivity toward value-added oxidation products, mainly formate and glycolate. These findings demonstrate the effectiveness of intrinsic nanostructure and interface engineering in achieving highly conductive, active, and potentially selective electrodes for anodic electrochemical reactions.

1. Introduction

The increasing global production of biodiesel as an alternative energy source is simultaneously introducing an excess of low-demand crude glycerol, initiating the requirement for its valorisation.[1–3] As sustainable technologies, electrochemical conversion systems provide a promising carbon-neutral route for synthesizing value-added products from waste glycerol at lower energy demands than traditional conversion technologies.[4,5] Additionally, further processing of glycerol *via* electrooxidation is energetically and economically competitive in comparison to both glycerol electroreduction and oxygen evolution reactions, where complete oxidation of glycerol to formic acid requires a small energy input of 0.69 V *vs.* RHE,[6] as well as the production of more valuable materials (*i.e.* oxygen and glycerol reduction products), making glycerol electrooxidation a promising alternative reaction in assistance of hydrogen evolution.[7–9] However, similarly to other electrochemical conversion technologies, glycerol electrooxidation is bottlenecked by the use of noble platinum-group metals as

---

Department of Chemical and Material Engineering, University of Alberta, Edmonton, AB, T6G 1H9, Canada. E-mail: jing.liu.arrow@ualberta.ca; mohajernia@ualberta.ca

† Electronic supplementary information (ESI) available. See DOI: https://doi.org/10.1039/d5ta00107b

catalysts characterized by their scarcity, high cost and poor stability during operation.[6,10,11]

As alternative electrochemical conversion electrodes, semiconductor metal oxides stand out as an abundant hence low-cost option *in lieu* of their noble counterparts, with high chemical and mechanical stability and morphological versatility.[12–14] Of these oxides, titanium dioxide is viewed as a promising contender due to its tuneable electronic properties and its opportunity of fabrication to various nanostructures.[15,16] Amongst various fabrication techniques, anodic self-growth of one-dimensional titania nanostructures aligns well with electrochemical applications. Anodization of Ti foil is performed in a fluoride-containing electrolyte, resulting in a directly coupled metal–metal oxide electrode with easily controlled oxide nanotube array morphology unlike powder-based morphologies.[17,18] This binder-free configuration allows for a direct e^- transfer pathway from the metal back-contact to the charge transfer layer, facilitating better charge separation and reducing resistances that result from the conventional addition of binder materials.[19,20]

Despite its corrosion resistance and stand-out electronic properties, TiO_2's performance is less studied in electrochemical contexts considering some bottlenecks such as having a wide bandgap of 3.0–3.2 eV that contributes to sluggish interfacial kinetics.[21] Additionally, the n-type semiconductor behaviour of TiO_2, hence its poor conductivity, highly limits electrooxidation applications due to current blockages in anodic operations.[22] As counter-measures, further treatments to improve the electronic properties of titania include metal decoration,[23–25] doping[26,27] and self-doping, which includes reduction-based treatments.[22,24] In terms of conductivity, semimetallic behaviour resultant of high temperature treatments was reported for titania, namely Magnéli/Ti_nO_{2n-1} phases, but is limited to nanoparticulate titania.[28–32] Hydrogen-based atmospheric treatments of TiO_2 in high temperature environments were reported to introduce point defects, namely oxygen vacancies (V_O) and Ti^{3+} sites ($O^{2-} + 2Ti^{4+} \rightarrow \frac{1}{2}O_2 + V_O + 2Ti^{3+}$), increasing charge carrier density, hence conductivity, due to ejected e^- into the titania lattice.[33,34] The characteristics of the point defect centres depend on the treatment operating conditions; defect types as well as their locations (surface exposed *vs.* lattice-embedded), with various catalytic activities, are concomitant of the temperature and annealing environment (*e.g.*, noble gas *vs.* H_2).[35] Anatase titania is also amphoteric in nature, with Ti^{4+}–O^{2-} acid–base Lewis pairs.[36] Considering glycerol oxidation, Yan *et al.* reported that the introduction of $M^{\delta+}$–V_O defects into the metal oxide catalysts can form frustrated Lewis pairs (FLPs). To form FLPs, $M^{\delta+}$ should be made more prone to receiving electrons and O more prone to lose electrons. This is where defect engineering titania forming Ti^{3+}–V_O comes into place, where oxygen vacancies possibly interacting with O-containing species and $M^{\delta+}$ sites facilitating C–C bond cleavage, hence a more efficient glycerol oxidation reaction mechanism.[37,38]

Additionally, co-catalyst decoration of titania nanotube arrays was reported to facilitate further electron transfer. Of different decoration techniques, direct "intrinsic" decoration on anodic TiO_2 nanotubes (NT) grown from Ti alloys with low concentration of noble metals, such as Au,[39] Pt,[40,41] Rh[42] and Ru,[23] allows for a uniform decoration of the tube walls with noble metal nanoparticles. The main advantage is the highly stable lodging of co-catalysts into the titania lattice in contrast with extrinsically decorated NT arrays.[39] Non-noble secondary metals such as Nb[43] or Cu[44] are reported to be simultaneously anodized, but instead of metal nanoparticles, they develop into doped secondary metal oxide sites within the NT lattice. In the case of copper, CuO_x-doped titania is especially well-studied for photoreduction applications, such as H_2 evolution and CO_2 photoreduction due to copper's plasmonic properties and its photocatalytic synergy with TiO_2. Despite this, the surface modifications introduced by copper decoration provide a promising premise for electrooxidation. Interestingly, synergistic effects between CuO_x and TiO_2 are reported, with Cu-doping partially promoting the formation of point defects in TiO_2 lattice.[45] Mechanistically, Wang *et al.* computationally demonstrated a possible link between the type of Cu decoration and point defects within the TiO_2 lattice, with interfacial Cu (higher stability in contrast to surface Cu) inducing more V_O formation by being an electron trapper, while simultaneously suppressing the formation of Ti^{3+}.[46,47] Additionally, the oxidation state of Cu-surface sites for both reactions is of various opinions within the literature, and the existence of Cu as either CuO–TiO_2 heterojunctions or Cu^0–TiO_2 Schottky junctions (noting that highly dispersed copper oxide NPs can also act as Schottky barriers) is under debate, although studies highlight the contribution of the treatment atmosphere to their phase, with decreasing oxidation states of Cu in more reducing environments (*e.g.*, H_2) as well as Ti^{3+}-induced reduction.[45,48–50] In the context of glycerol electro-oxidation, Although Cu-based electrocatalysts were reported to exhibit low onset potentials, pristine Cu and Cu oxide glycerol oxidation electrocatalysts suffer from compromised durability, where Cu oxides suffer from intrinsic low conductivity, and metallic Cu can suffer from structural collapse, as well as its susceptibility of leaching in the presence of glycerol.[51–54]

In this paper, we spotlight the synergistic interactions between Cu and TiO_2 point defects ensuing surface modifications of the semiconductor through the lens of electrochemical glycerol oxidation. We fabricated intrinsically doped Cu–TiO_2 nanotube arrays, treated them in a H_2-based high temperature environment, and explored the links between intrinsically lodged $Cu^{\delta+}$ sites and induced Ti^{3+}/V_O defects electrochemically and spectroscopically. Additionally, we briefly demonstrate the effect of doping the titania-based electrodes with a co-catalyst on the electronic configuration of CuO_x–TiO_2 NT arrays using cobalt as an example, and the resultant synergistic interactions between intrinsically embedded Cu and deposited Co species, showing the contribution of the former in uplifting the performance of deposited catalytic species from effective zero current density to a 35 times increase as Cu is intrinsically embedded into the titania nanotube walls, and about 900 times increase when deposited on reduced Cu-doped titania nanotube arrays (CuTNAs).

2. Experimental details

2.1. TiO_2 NTs preparation

TiO_2 nanotube arrays and Cu-decorated nanotube arrays were fabricated *via* anodization of Ti foil (0.125 mm thick, Hauner Metallische Werkstoffe), and Ti–Cu foils with different Cu concentrations (3, 5 and 8 at%) [0.5 mm thick, Hauner Metallische Werkstoffe]. Ti foil pieces were cut into 1.5 mm × 1.5 mm squares and mechanically polished using 1200 grit SiC papers. The foils were then ultrasonically cleaned sequentially in reagent alcohol (90% ethanol, 5% methanol, 5% isopropyl alcohol; Fischer Chemical) and deionized water for 10 minutes each. The foils were air-dried then anodized at 60 V using a DC power supply for 15 minutes in a 0.15 M NH_4F ethylene glycol (3 vol% deionized water) electrolyte, in a two-electrode configuration with a graphite rod as a counter electrode. The resultant anodized samples were then dipped in reagent alcohol for 60 minutes, then air-dried. The fabricated anodic nanotube samples were air annealed to crystallize the amorphous TiO_2 into anatase nanotubes in a box furnace (Thermolyne, Model No. FB1415M) at 450 °C for 1 hour, then cooled rapidly in ambient temperature. Resultant TiO_2 nanotubes (TNA) and Cu-decorated nanotubes (CuTNA) were treated in a sliding tube furnace (Barnstead-Thermolyne, Model No. F21100) in the presence of H_2/Ar (10 : 90) environment, at temperatures ranging from 350 °C to 500 °C, at a flow rate of 50 cc min^{-1}. To study the synergistic effects as a result of Cu-decoration, cobalt nanoparticles were embedded on the reduced TNA nanotube samples *via* electrodeposition at cathodic voltage of 1 V using a DC power supply in 0.5, 5 and 50 mM $Co(NO_3)_2$ for 15 minutes, then washed in deionized water and air-dried.

2.2. Characterization of surface-engineered TNAs

The surface morphology of TNA samples was studied using field-emission scanning electron microscopy (FESEM, Hitachi S-4800) with an 8 mm working distance and 10 kV accelerating voltage, and transmission electron microscopy (TEM, JEOL JEM-ARM200CF) at 200 kV HT, as well as elemental analysis using an energy dispersive X-ray detector. The crystal structure of the pristine and Cu-decorated TNAs and fabricated nanotubes was interpreted using Rigaku Ultima IV X-ray diffractometer (Cu Kα, 1.5406 Å, 44 mA, 40 kV) with a 2θ range of 20–80° with a 1° glancing angle at a step size of 0.01°. X-ray photoelectron spectroscopy (XPS, Kratos AXIS Ultra) was used to characterize the surface composition and chemical states of various samples with the C 1s binding energy peak calibrated at 284.8 eV.

2.3. Electrochemical performance of TNAs

Electrochemical properties and impedance-based characteristics were elucidated using a 3-electrode setup in 1 M KOH + 0.1 M glycerol electrolyte, with TNA substrates as the working electrode (surface area 0.785 cm^2) with a Pt rod counter electrode, and Hg/HgO (1 M KOH) served as a reference electrode. Half-cell electrochemical performance of titania nanotube-based electrodes are performed using a Solartron 1287 electrical workstation. Linear sweep voltammetry tests were performed from 0 V to 3 V *vs.* RHE at a 1 mV s^{-1} scan rate. Cyclic voltammograms were obtained at different scan rates (20–100 mV s^{-1}, 10 cycles) from 0.025 V to 1.3 V. Impedance-based tests were performed using BioLogic SP-200 electrochemical workstation. Electrochemical impedance spectroscopy (EIS) analyses were performed at a DC voltage of 0 V *vs.* OCP, 10 mV AC voltage in a frequency range of 100 kHz to 100 mHz. Mott–Schottky analysis was performed in DC voltage range of −1 V to 1 V *vs.* RHE at a frequency of 200 Hz. The measured potential was converted to the RHE scale using the following equation derived from the Nernst equation:[55]

$$E_{\mathrm{RHE}} = E_{\mathrm{Hg/HgO}} + 0.059\mathrm{pH} + E^{0}_{\mathrm{Hg/HgO}} \qquad (1)$$

where E_{RHE} is the potential *versus* reference hydrogen electrode in volts (V), $E_{\mathrm{Hg/HgO}}$ is the potential measured *via* the electrochemical workstation *versus* Hg/HgO reference electrode and $E^{0}_{\mathrm{Hg/HgO}}$ is the standard Hg/HgO reference electrode potential at 298 K equivalent to 0.098 V *vs.* RHE.

3. Results and discussion

Herein, the performance of Cu-doped TiO_2 nanotube arrays (CuTNAs) is investigated in the context of electrocatalytic glycerol oxidation. Self-aligned TiO_2 nanotubes are grown *via* high-voltage anodization in ethylene glycol containing 0.15 M NH_4F and 3 vol% water forming a layer of amorphous TNAs, which is followed by annealing in air to crystallize into anatase TiO_2 (see Fig. S1† for the colour change post-treatment). Ti–Cu alloy substrate foils containing a range of atomic concentrations of Cu (0–8 at%) were anodized and investigated. The use of alloys as metal substrates helps in the organized intrinsic embedding of Cu into the length of the TiO_2 nanotubes as anodic growth proceeds. Fig. 1 shows the morphological trends between pristine TNAs (p-TNA) and Cu-decorated TNAs with different concentrations. In pristine TNAs, the outer tube diameter is an average of 99.3 ± 12.5 nm wide with a wall thickness of 19.8 ± 2.3 nm and a nanotube length of 6.8 ± 0.2 μm. The addition of Cu into the metal foil substrate, and the subsequent anodization, demonstrated a slight decrease in the nanotube dimensions, with an outer diameter of 79.4 ± 5.7 nm and a thickness of 15.7 ± 2.5 nm for 3 at% Cu, with comparable dimensions for other Cu at% concentrations (Table S1†). Lengthwise, however, the tube length follows a negative trend with increasing Cu at%. Increasing concentrations of Cu in the original metal foil correlates to the formation of more Ti_2Cu intermetallic sites which, unlike Ti, do not undergo a regular anodic oxide growth pattern and hinder the self-assembly of TNAs. At a Cu concentration of 8 at%, the growth is significantly impeded peaking at ≈4 microns [Fig. 1(d)], with areas of impeded anodic growth and various "volcanic" pits in Fig. 1(e) are observed in the top morphology of the arrays. Fig. 1(f) shows an area with smooth oxide regions (yellow dotted boxes) as well as premature growth of nanotubes, along with the "pits" [red circles in Fig. 1(e)], signifying areas where the anodization process halts.[44] SEM-EDX results (Fig. S2 and Table S2†) show the disparity

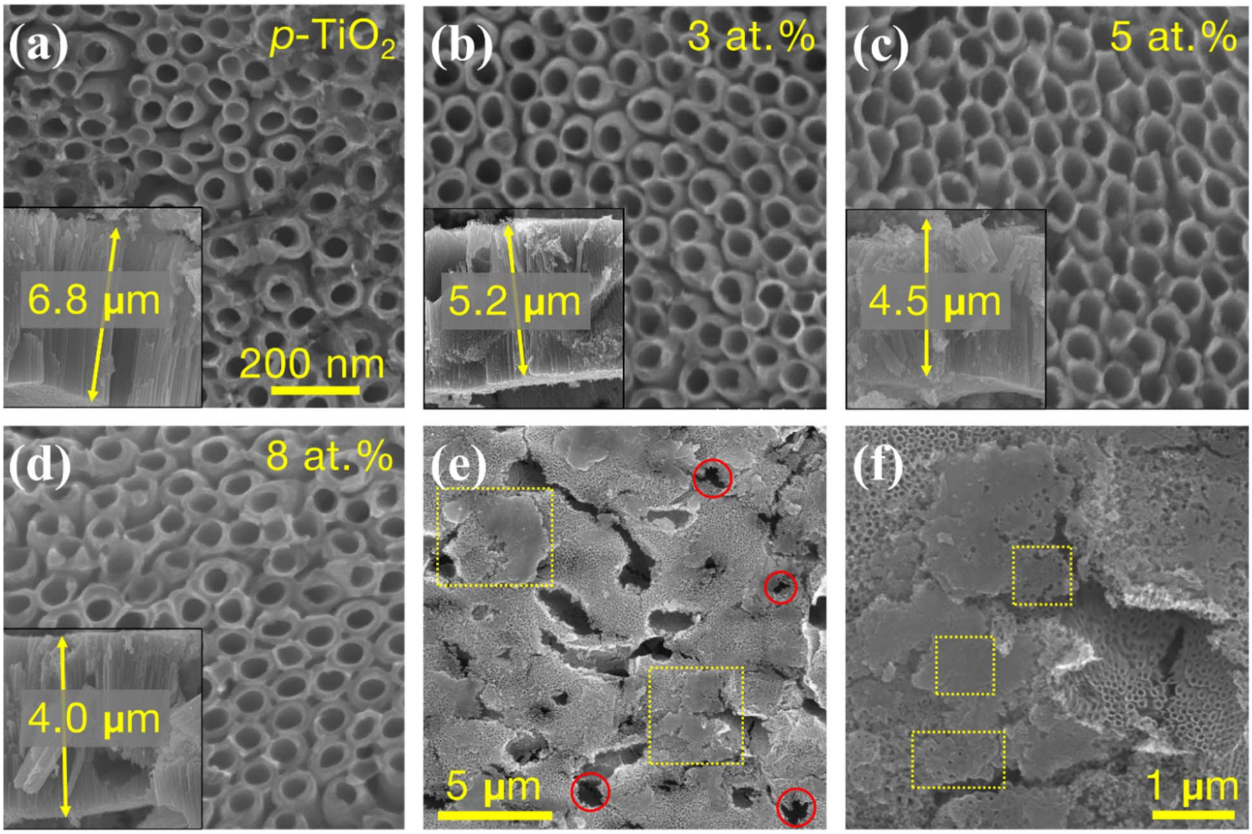

Fig. 1 FESEM images of (a) anodic titanium dioxide nanotubes, (b) 3-CuTNA, (c) 5-CuTNA, (d) 8-CuTNA, (e) top view of anodic 8-CuTNA and (f) growth-impeded areas in 8-CuTNA.

between the Cu concentrations in the metal substrate *versus* in the nanotube arrays, with a significant decrease due to the formation of intermetallics as the Cu concentration peaks at 0.58 at% in TNAs grown from 8 at% Cu Ti alloys. Additionally, Cu is uniformly distributed along the nanotube walls as seen in the EDS maps in Fig. S2(e),† where the Cu is simultaneously doped into the tube walls as the oxide nanotube arrays grow during anodization. Fig. 2(a) shows X-ray diffraction analysis conducted to further investigate the anodic TNAs. Anatase peaks in annealed pristine TiO$_2$ can be seen at around 25.31° (101), 36.36° (103), 38.34° (121), 62.83° (204), 70.66° (202) and 76.16° (301) [ICDD 96-900-8215]. For Cu-doped samples, there were no apparent peaks for Cu or Cu oxides, predominantly due to their low concentration that is below the detection limit of XRD. However, peak shifts to lower angles for anatase peaks [Fig. 2(b)] were observed, with a large shift at 8 at%, which is attributed to the expansion of the oxide lattice due to Cu inclusion. Ti peaks corresponding to the metal foil that back-

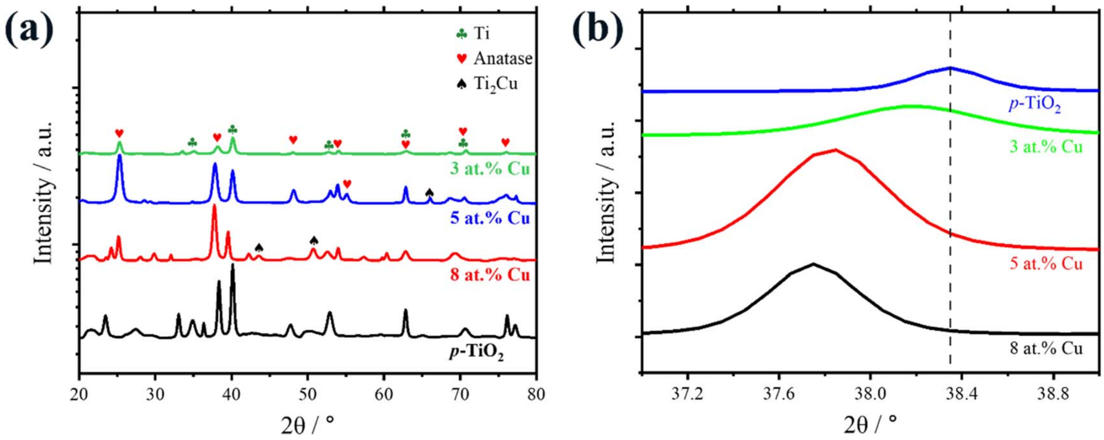

Fig. 2 (a) XRD pattern of pristine, 3, 5, and 8 at% anodized Ti foils and their (b) resultant peak shifts.

contacts the anatase TNAs appear at 34.88° (100), 40.14° (110) and 52.88° (120) [ICDD 96-900-8518], and at higher concentrations of Cu in the metal foil, faint peaks corresponding to Ti_2Cu intermetallic phases are observed at 43.57° and 50.71°.[56] XRD patterns in Fig. S3(a) and (b)† showed that high temperature hydrogen treatment of anatase TNAs does not seem to cause significant shifts of TiO_2 peaks, as well as no significant observed morphological changes to the TNAs such as any compromise to the structural integrity of the tubes [Fig. S3(c) and (d)†], essentially demonstrating that the induced change is mainly to the electronic properties of TiO_2.

Steady state polarization curves [Fig. 3(a)–(c)] were recorded for a comparative analysis between different surface-modified TNAs from a glycerol electrooxidation perspective. As pristine TiO_2 is an n-type semiconductor, it suffers from a current blockage in the anodic direction, imposing a challenge for oxidation reactions. Air annealed TNAs (a-CuTNA) exhibit typical TiO_2 behaviour as reflected by effective zero current densities even at large applied voltages (3.0 V *vs.* RHE), regardless of the concentration of Cu [Fig. S4(a) and (b)†]. Upon treatment in hydrogen at elevated temperatures, the resultant current density increases, peaking at a maximum of 7.75 mA cm^{-2} at 3.0 V *vs.* RHE post-treatment for hydrogen-treated CuTNAs (H-CuTNA) at 500 °C. The performance starts dropping at 550 °C, and at 600 °C the oxide layer becomes highly brittle and breaks apart upon polarization. For different concentrations of Cu in the metal substrate (Fig. S4†), the performance drops at higher at% due to the inhibition of nanotube growth during anodization, as well as the formation of pits in intermetallic sites. The intrinsic kinetic activity of the different TNAs is limited by the first electron transfer step, with pristine TNAs having significantly high Tafel slopes at 1255 mV dec^{-1} due to its extremely low conductivity and high Schottky barrier in anodic voltages [Fig. 3(b)]. Although the addition of Cu improves the kinetic activity, only at further reduction does the Tafel slope show a significant decrease to 381 mV dec^{-1} at

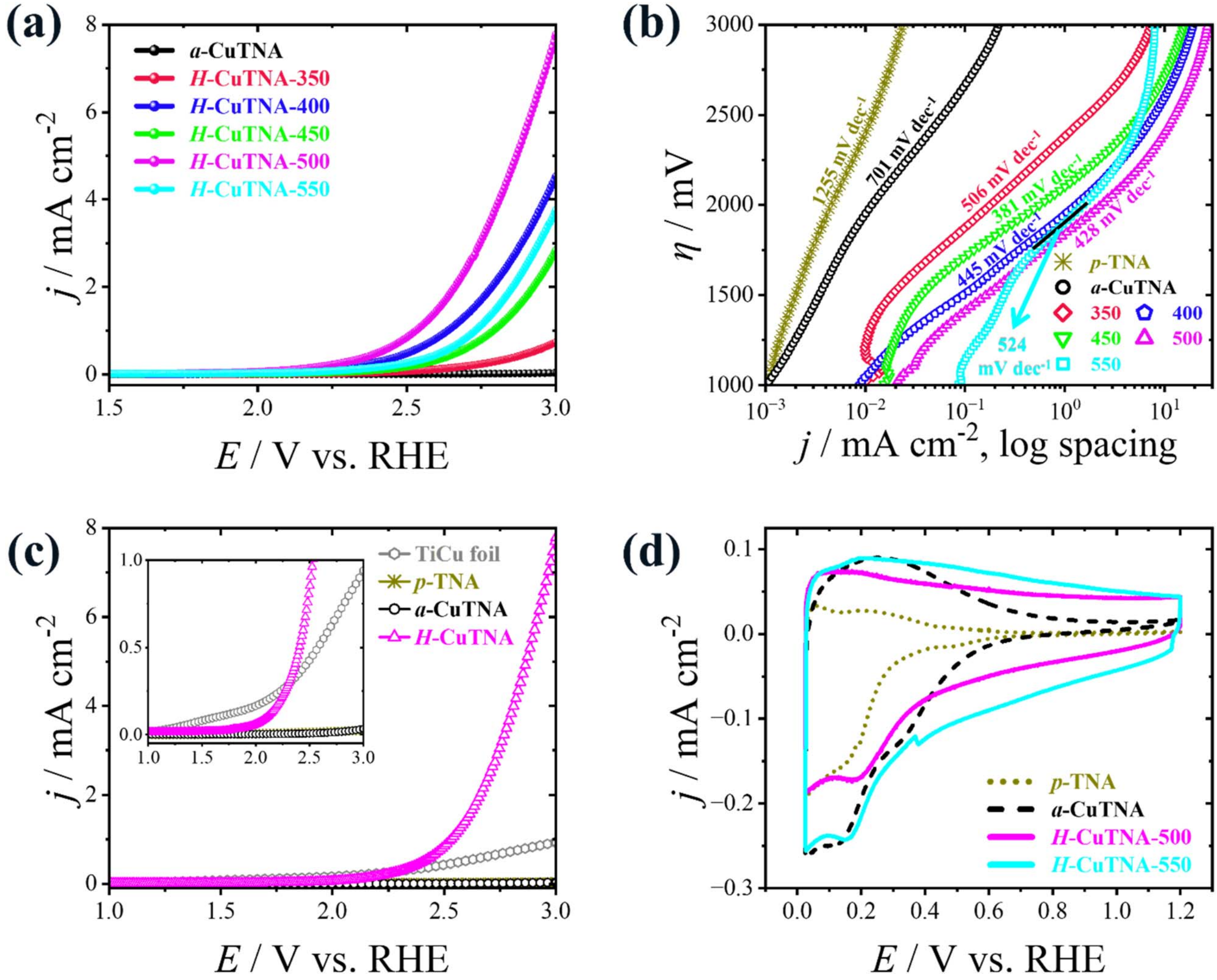

Fig. 3 (a) Polarization curves of anodic Cu-decorated (3 at%) TNAs hydrogen-treated at different temperatures (350, 400, 450, 500 °C) and air annealed CuTNA recorded in 1 M KOH + 0.1 M glycerol at a sweep rate of 1 mV s^{-1}. (b) Tafel plots of high-temperature hydrogen-treated CuTNAs. (c) Polarization curves recorded in 1 M KOH + 0.1 M glycerol at a sweep rate of 1 mV s^{-1} of TiCu foil, and TNAs with different treatments (pristine, Cu-decorated, hydrogen-treated). (d) Steady-state cyclic voltammograms of TNAs with different treatments (pristine, Cu-decorated, hydrogen-treated) in 1 M KOH + 0.1 M glycerol at a sweep rate of 100 mV s^{-1}.

450 °C. At high overpotentials (>2.5 V *vs.* RHE) the performance degrades rapidly as the reaction profile becomes mass transfer-limited, with a drawn-out deactivation process. To further study catalyst deactivation, we performed a chronopotentiometric stability test at mild conditions of 1 mA cm^{-2} for 8 hours [Fig. S5(a)†], which showed significant performance loss with an overpotential increase of >1 V *vs.* RHE. The post-stability FESEM images show that deactivation of the TNAs is less likely due to pore blockage [see Fig. S5(b)–(d)†] and is possibly due to the rapid saturation of the adsorbed reactant glycerol and possible products on the array surface, as well as the uprooting of some nanotube array structures from the metal foil. In case of possible re-oxidation, it is possible that some Ti^{3+}/V_O sites have re-oxidized, however we did not observe a significant complementary color change to a lighter grey in the sample for complete re-oxidation.[57] For vigorously doped CuTNAs at 550 °C, tunnelling breakdown of the Schottky barrier (>3 V *vs.* RHE) can accelerate the deactivation process.[58] The performance of the TNAs was compared against freshly polished and ultrasonicated TiCu foil [Fig. 3(c)], showing a current blockage for the latter. Although more conductive, the high surface area of TNAs enables an improved electrochemical performance. However, the increased surface area is insufficient for pristine TiO_2, and it is only upon high temperature reduction of the CuTNAs when the resultant current density surpasses that of TiCu foil at 2.3 V *vs.* RHE. Additionally, pristine TiO_2 fails to perform as a glycerol electrooxidation catalyst, even post-reduction in aggressive H_2 environments to improve its conductivity. As it struggles to reach 1 mA cm^{-2} of current density at high voltages of 3 V *vs.* RHE [Fig. S4(c)†], it shows the necessity of doping with a more active component. Despite the slight increase in current density relative to strictly air annealed p-TNA, reduced p-TNA falls short of reduced CuTNAs by exhibiting a higher onset potential of 2.06 V *vs.* RHE, whereas the polarization curve of reduced CuTNA onsets at 1.93 V *vs.* RHE.

The chronopotentiometry testing was carried out at 1 mA cm^{-2} to analyze and quantify the resulting products for pristine TNA, and strictly air annealed and reduced CuTNA, along with their Faradaic efficiencies. Two electrolyte extractions of one millilitre each were performed during an 8 hour test, one at the 4-hour mark and one at 8-hours to be analyzed by nuclear magnetic resonance (NMR) spectrometer. The ^1H NMR spectra for 4-hour and 8-hour samples were obtained (Fig. S6(a) and (b),† respectively), showing the existence of mainly glyceric acid, lactic acid, glycolic acid and formic acid peaks. Faradaic efficiency values for different electrodes was calculated using the method indicated by Yelekli Kirici *et al.*[59] Pristine TNAs show the lowest production and faradaic efficiency, as it ends at the 8-hour mark with an efficiency of 0.86%, a drop from 3.16% possibly due to mass transfer limitations and subsequent breakdown of the products, and it struggles to convert the lactic acid to formic acid, while still maintaining a small concentration of glyceric acid, showing the conversion of glycerol through a glyceraldehyde route. The addition of Cu to the metal substrate enables the TNA-based electrode to convert more lactic acid to glycolic and formic acids, while still maintaining a low Faradaic efficiency of 3.12%. Upon reduction of CuTNA, the lactic acid production peaks at the 4-hour mark, with 1.17 mM produced, as well as an increase in the glycolic acid production from air annealed samples at a concentration of 1.73 mM. The Faradaic efficiency of H-CuTNA is reported to be 7.73% at 8-hours, a slight drop from 8.73% at 4-hours, with the total produced formic acid being at 2.99 mM.

Using steady state cyclic voltammetry [Fig. 3(d)], the physicochemical characteristics of the charge transfer layer were evaluated. The cyclic voltammogram of titania is comprised of faradaic processes at cathodic potentials with a large pseudocapacitive profile, and non-faradaic processes at anodic potentials greater than the flat-band potential of the TNAs representing the start of the electron depletion zone.[60,61] In the cyclic voltammogram for p-TNAs, this corresponds to a slight cathodic peak at around 0.46 V *vs.* RHE. The addition of Cu to the nanotubes shifts back the peak to around 0.36 V *vs.* RHE, which was comparable to the flat-band potential extracted from Mott–Schottky measurements [see Fig S6(b)†].[60] Despite the shift of the flat-band potential to lower potential for Cu-TNA, its kinetic performance as evaluated by Tafel analysis does not deteriorate. This alludes to the suppression of Ti^{3+} electron trapper site formation but not that of oxygen vacancies.[46] Upon the hydrogen-treatment of the Cu-TNAs, the trapper site peak shifts to higher potentials. Post-treatment at 500 °C, the trapper site peak disappears as the voltammogram's capacitive region starts to expand, and at 550 °C the reduction peak starting at 0.025 V *vs.* RHE (characteristic of Ti^{3+} sites) increases considerably. For pristine TNAs [Fig. S4(d)†], reduction at 500 °C expands the trapper site peaks as well as shifts it to higher oxidation potentials, without disappearing in similar fashion to CuTNA. The voltammogram expansion, however, does not contribute significantly to the electrochemical performance of the electrode, with persisting electrocatalytic limitations as discussed earlier with respect to the polarization curve.

Electrochemically active surface area (ECSA) analysis was performed at a scan rate range of 20 to 1000 mV s^{-1} at 1.1 V *vs.* RHE as seen in Fig. S8† For pristine TNAs, and both air annealed and reduced CuTNAs, the non-faradaic regions (>0.46 V *vs.* RHE) exhibit a symmetric profile, which corresponds to a linear plot of $\Delta j_{1/2}$ *vs.* scan rate. The slope of the aforementioned plot describes the interfacial capacitance (C_{dl}), and the ECSA was calculated by dividing the C_{dl} by the specific capacitance (C_s) of TiO_2 (0.04 mF cm_{bulk}^{-2}).[62] The intrinsic decoration of titania and the subsequent reduction increases the C_{dl} of the arrays and consequently the active surface area increases by about two orders of magnitude from 0.176 cm^2 cm_{bulk}^{-2} for pristine TNAs to 10.4 cm^2 $cm^{-2}{}_{bulk}$ at 550 °C (Fig. S9†). To further investigate the interface characteristics, electrochemical impedance spectroscopy measurements were employed.

The obtained Nyquist plots [Fig. 4(a)] and their corresponding Bode plots (Fig. S10 and S11†) were used to fit equivalent two-time constants circuits, with two semicircles corresponding to space charge layer and the array-electrolyte interface at high and low frequencies respectively. In this work, the equivalent circuit fitting utilized constant phase elements Q_{CPE}, where

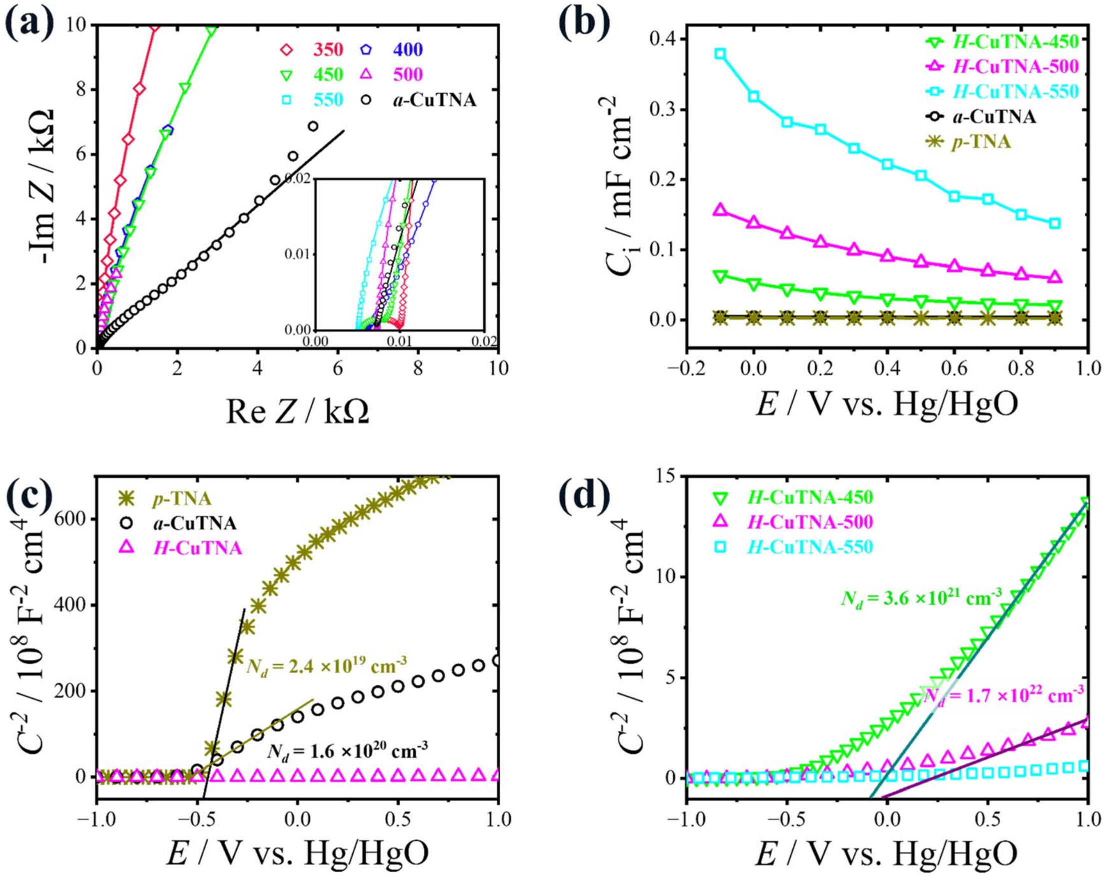

Fig. 4 (a) Nyquist plots of annealed and d at different temperatures (350, 400, 450, 500, 550 °C) Cu-decorated (3 at%) TNAs recorded at an AC voltage of 10 mV in 1 M KOH + 0.1 M glycerol. (b) Electrode–electrolyte interface capacitance *vs.* applied DC voltage plot for air annealed and reduced CuTNAs. Mott Schottky plots at $f = 1000$ Hz for (c) pristine TNAs, CuTNAs and hydrogen-treated CuTNAs and (d) hydrogen-treated CuTNAs at 450, 500 and 550 °C.

impedance $Z_{\mathrm{CPE}} = [Q_{\mathrm{CPE}}(i \cdot \omega)^{\alpha}]^{-1}$ to account for deviations from ideal capacitive behaviour $\alpha = 1$ caused by interfacial heterogeneities on the electrode surface (ESI Note 1†).[63] The impedance plots distinctly show that strictly air annealed TNAs are represented by circuits with a ladder configuration $R_s(Q_{sc}[R_{sc}(-R_iQ_i)]$ as the depletion zone extends through the entire tube wall to the metal foil-oxide interface, with the charge transfer processes being predominantly influenced by the space charge layer (SCL) charging/discharging.[64] The large SCL resistances R_{sc} of p-TNAs and a-CuTNAs, 43 and 1.3 kΩ respectively (Table S4†), hence their low C_{sc} values (Table S5†), are attributed to the height of the Schottky barrier. Additionally, as Ti^{3+} centres serve as both electron trappers and catalytic active sites, their low concentration in air treated samples increases the interfacial resistance as the electrode depends solely on electrons in the space charge layer for kinetic processes. As the samples are thermally treated, the plots of reduced samples fit better into a Voigt configuration $R_s(Q_{sc}R_{sc})(R_iQ_i)$ with smaller and more distinct high frequency semi-circles at lower atmospheric reduction temperatures, coinciding with the thinning of the SCL and the increase of the conductivity caused by the release of electrons from Ti^{3+}/V_O formations into the titania lattice. As the treatment temperature increases, the semi-circle shrinks until disappearing completely at 550 °C. Post-high treatment temperatures, the charge transfer profile is dominated by Ti^{3+} active sites, and the charging capacity of the space charge layer increases significantly. Hence, the charge transfer resistance at the interface R_i decreases, reaching a value of 22 kΩ at 550 °C reduction. Table S5† compares the interfacial capacitance values obtained *via* cyclic voltammetry analysis *versus* impedance spectra. There is a loose agreement between the techniques in the increasing trend of capacitance with higher H_2 treatment temperatures. Cyclic voltammetry, however, generally reports smaller capacitance for reduced samples as it introduces a larger potential perturbation to the charge transfer layer, which is more likely to cause a loss of some Ti^{3+} centres *via* re-oxidation.[65,66] For pristine titania, as the interfacial capacitance is heavily influenced by the space charge layer behaviour, the extremely low space charge layer capacitance limits the chare transfer profile at the electrode–electrolyte interface.[24]

Fig. 4(b) explicates the changes in interfacial capacitance *versus* applied potential to account for interfacial perturbations obscured by static impedance analysis. The plot was extracted from multiple potentiostatic impedance spectra shown in Fig. S12† for potentials ranging from −100 to 900 mV *vs.* Hg/

HgO. The capacitance shows an exponential profile towards the cathodic directions, characteristic of an n-type semiconductor, with plateauing at higher potentials. Clearly, higher oxidation potentials show limited capacitance, and the exponential trend is consistent for the different treated samples. To elucidate and compare the changes in dopant concentrations in different TNA samples, Mott Schottky plots were obtained at a frequency of 1000 Hz between 1 V to −1 V *vs.* Hg/HgO [Fig. 4(c)–(d)]. To calculate the charge carrier concentration in the TNAs, the following equation was used:[67,68]

$$N_{\mathrm{d}} = \left(\frac{2}{\varepsilon_0 \times \varepsilon_{\mathrm{r}} \times e}\right)\left[\frac{\mathrm{d}\left(C_{\mathrm{i}}^{-2}\right)}{\mathrm{d}E}\right]^{-1} \quad (2)$$

where ε_0 is the permittivity of free space equivalent to 8.85 × 10^{-12} F m^{-1}, ε_{r} is the relative permittivity of TiO_2 at 31, e is the elementary charge at 1.60217663 × 10^{-19} coulombs, C_{i} is the interfacial capacitance and E is the applied potential. Typical of an n-type semiconductor, p-TNA is characterized by a large positive slope with a dopant concentration of 2.4 × 10^{19} cm^{-3}. As the TNAs are intrinsically Cu-decorated, the slope decreases giving a dopant concentration of 1.6 × 10^{20} cm^{-3}. Typically, electron trapper Cu is expected to lodge into the titania lattice in its oxide form (CuO_x), forming p–n junctions.[69] Albeit promoting the formation of oxygen vacancies, hence increasing the electrons released into the lattice, the concentration of Cu dopants is not sufficient to improve the kinetic activity, with additional suppression of Ti^{3+} centres.[47] As the treatment temperature increases, the charge carrier density of CuTNAs increases significantly. The slope is seen to decrease by 2.5–3.5 times with each 50 °C increase [Fig. S7(a) and (c)†] and at 550 °C, the charge carrier density of CuTNAs experiences a ≈200 times increase from a-CuTNAs to 3.9 × 10^{22} cm^{-3}. Additionally, the flat band potential of the CuTNAs increased by 1.0 V from 0.37 V *vs.* RHE for a-CuTNAs to 1.37 V *vs.* RHE for H_2-treated CuTNAs at 550 °C [Fig. S7(b)†], showing a decrease in electron depletion which signifies a thinning space charge layer, which complements the previously discussed cyclic voltammetry findings. Table S3† summarizes the key Mott–Schottky analysis parameters for each temperature of reduction.

To further explain the effects of Cu decoration and atmospheric reduction on Cu-TNAs, high resolution transmission electron microscopy (HRTEM) along with selected area electron diffraction (SAED) were employed to evaluate the fine structure of hydrogen-treated CuTNA treated at 500 °C. Lattice fringes on the nanotube walls [Fig. 5(a)] with an interplanar distance of 0.365 nm correspond to anatase titania, but no fringes corresponding to CuO_x were detected, showing the trace concentrations of Cu on the tube walls. The SAED pattern [Fig. 5(b)] shows a predominant presence of anatase with no peaks corresponding to CuO_x or reduced titania phases. However, high-angle annular dark field (HAADF) analysis, along with electron dispersive X-ray (EDX) spectroscopy (Fig. S13†) demonstrated the uniform distribution of both small copper-predominant nanoparticles, as well as embedded copper oxide along the tube wall. In Fig. 5(d), the tube edge from Fig. 5(c) was elementally mapped *via* EDX, and clear copper-predominant nanoparticles with a diameter of 2.3 ± 0.35 nm were observed. Additionally, perforations along the nanotube walls were observed on Fig. 5(c), which are mainly attributed to the burn-off of carbon that mainly results from anodization in organic electrolytes during the air annealing process.

The chemical state of different species on the surface of the nanotube arrays, as well as the atomic surface composition, was investigated using XPS analysis. Fig. 5(e) depicts the survey

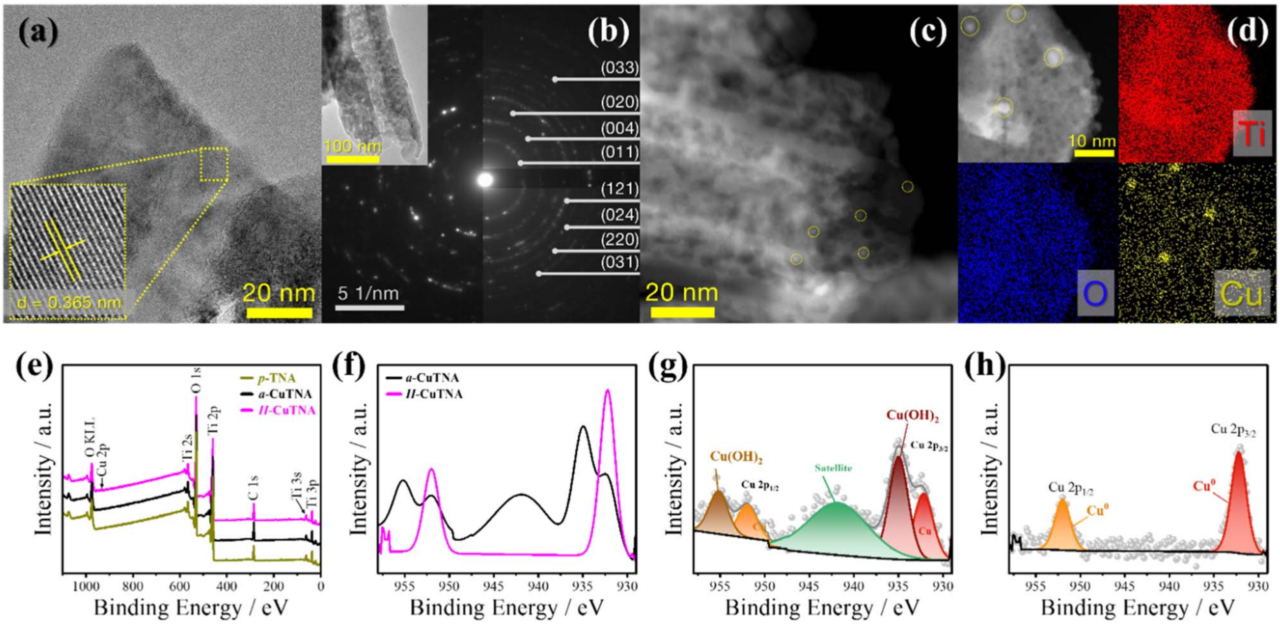

Fig. 5 (a) HRTEM image of H-CuTNA nanotube edge and (b) SAED pattern of polycrystalline Cu-decorated nanotube. HAADF-STEM image of (c) H-CuTNAs and (d) nanotube edge with corresponding EDS mapping of Ti, Cu and O. (e) Survey XPS spectra of p-TNA, a-CuTNA and H-CuTNA, (f) high-resolution XPS spectra of Cu 2p for a-CuTNA. Deconvoluted HR-XPS spectra for (g) a-CuTNA and (h) H-CuTNA.

spectra for pristine TNAs, and air annealed and H_2-treated Cu-TNAs. The XPS survey results show the predominant presence of Ti, O, and adventitious carbon, as well as the slight presence of Cu for both Cu-TNA samples. An overlay of Cu 2p high resolution XPS spectra for both a-CuTNA and H-CuTNA [Fig. 5(f)] show the effects of optimized reduction treatment on changing the oxidation state of nanotube wall-embedded Cu. As the CuTNAs are reduced, the major satellite peak is seen to disappear, and the chemical state of Cu shifted to a lower binding energy, indicating the formation of Cu/Cu_2O sites, as observed in the HAADF images in Fig. 5(d) and in Fig. S13,† although some prominent metal nanoparticles are present, Cu is well-distributed along the nanotube walls. Interestingly for a-CuTNAs, the deconvoluted Cu 2p HR-XPS spectra [Fig. 5(g)] shows the presence of both Cu^+ (peaks 932.2 eV and 951.95 eV) as an oxide, and hydroxyl Cu^{2+} (peaks 934.98 eV and 955.19 eV). The latter oxidation state was supported by the complementary O 1s HR-XPS (Fig. S14†) as the hydroxide deconvoluted peak at 531.4 eV represents 33.7 at% of surface oxygen. As both spectra are expected to exhibit satellite peaks, it is difficult to attribute the observed peak at 941.77 eV to one oxidation state of Cu. XPS analysis of Cu species post-hydrogen treatment show doublets at 932.21 and 952 eV respectively which is attributed to Cu^0 (*i.e.* metallic) species, showing the effect of H_2 treatment in reducing Cu species to Cu metal and the removal of hydroxide groups from the surface. The Cu surface atomic concentration using XPS analysis was found to be 0.36% (Table S6†), which is slightly higher than SEM-EDX results (0.24 at%), but lower than the concentration of the TiCu substrate of 3 at%. We further analyzed the Cu concentration in 3 at% Cu-TNA using atomic absorption spectroscopy (AAS), with 1.48 at% Cu reported. The contrast between XPS and AAS shows that the oxidation rate of Cu during the anodization process is much slower than that of Ti, allowing more Cu to be embedded at the bottom end of the TNAs than in the surface. In Fig. S14,† for pristine TNAs, and air annealed and reduced CuTNAs alike, the deconvoluted Ti 2p high resolution XPS spectra show Ti^{4+} doublets corresponding to the metal oxide, and the O 1s peaks show the presence of lattice oxygen, and peaks at 531.1 ± 0.2 and 532.1 ± 0.2 eV corresponding to hydroxyl groups and adsorbed H_2O respectively. The latter is rather adventitious due to the interaction of atmospheric water vapor on defect sites prior to *ex situ* XPS.

To evaluate the performance of the optimized Ti–Cu electrode as a support material we studied the resultant synergistic effects of adding a secondary metal on the TNA surface by electrodepositing Co at a cathodic DC voltage of 1 V in $Co(NO_3)_2$ precursor solution of different concentrations, with a graphite rod as a counter-electrode. Three concentrations of Co precursor were tested, namely 50, 5 and 0.5 mM. Fig. S15(a)† shows a polarization curve demonstrating the correlation between decreasing concentrations and enhanced glycerol electrooxidation performance. Co electrodeposition demonstrates a sharp decrease in the reaction onset of the TNAs, with the smallest onset observed with the use of 5 mM Co precursor solution. Additionally, for Co(5 mM)@H-CuTNA, a prominent CoO/Co_3O_4 peak at 1.84 V *vs.* RHE is observed. The subsequent glycerol oxidation reaction profile is almost immediately impeded and mass transfer-limited leading to a plateauing starting from 2.5 V *vs.* RHE. Decreasing the electrodeposition concentration to 0.5 mM extends the kinetic GEOR region, despite the concentration polarization taking over at voltages higher than 2.25 V *vs.* RHE. NMR spectrometry for 0.5 mM Co-doped H-CuTNA show a fascinating increase in product concentration [Fig. S6(c) and (d)†], as the amount of formic acid significantly increases from 2.99 mM to 9.63 mM, with a full conversion of lactic acid to formic and glycolic acid (at a concentration of 1.29 mM). The resultant Faradaic efficiency reaches up to 33.68% at the 8-hour mark from 7.73% for H-CuTNA [Fig. S6(e)†]. Additionally, the addition of Co to H-CuTNA allows it to experience an increasing faradaic efficiency with time, showing that more glycerol is being converted into its products with decreased mass transfer limitations.

Interestingly, FESEM analysis of 0.5 mM show no visible Co species compared to the relatively large Co-based agglomerations for 50 mM [Fig S16†], signifying particle size selectivity. X-ray diffraction patterns for different cobalt concentrations are displayed in Fig. S17.† Although there are no significant Co peaks, a slight peak shift of the 38.3° anatase peak is observed upon Co doping, showing a possible incorporation into the crystalline anatase structure. The SEM-EDX analysis in Fig. S18† show minimal amounts of Co electrodeposition, showing the effect of trace elements in effectively improving the electrode performance *via* the synergistic properties induced by modifying the Cu-CoO_x d-band center.[70] Table S8† shows an increasing pattern of Co at% with increasing precursor concentration, with 0.59 at% of Co detected post-treatment in 50 mM of cobalt(II) nitrate. HRTEM imaging (Fig. S19†) show no significant loading of CoO_x particles especially in the core of the tube arrays compared to the tube edges. The deposited CoO_x prevails mostly on the top surface of the arrays, facilitating Cu activity. Fig. 6(a) compares between Co deposition on different surface-modified TNAs for a cobalt precursor concentration of 0.5 mM, with the corresponding Tafel plots in Fig. 6(b). For pristine TNAs, the deposition of Co provides minimal contribution, with an effective zero current density at up to 3 V due to its previously discussed charge transfer limitations. However, for CuTNAs, there is a distinct increase in the current density with an observed $Co^{\delta+}$ oxidation peak after the onset of 1.40 V. As observed in the corresponding Tafel plot [Fig. 6(b)], all tested electrodes are kinetically limited by the first electron transfer step, which correlates to the Tafel slope at the onset for each sample. Upon the intrinsic Cu-decoration of TNAs, the second slope decreases from 184 to 129 mV dec^{-1}, and its kinetic profile is observed to extend to a current density two-orders of magnitude higher. For Co@TNA, three distinct slopes are observed, while for Co@CuTNA (*i.e.* regardless of atmospheric treatment), there are four distinct slopes, each designating a possible reaction step forming a glycerol oxidation intermediate. For H_2 treated CuTNAs, Co deposition was observed to reduce the overpotential by 845 mV at 5 mA cm^{-2}. At the onset of 1.37 V *vs.* RHE, the electrode exhibits a substantial slope of 1654 mV dec^{-1}, signifying that the electrode is kinetically limited by the first electron transfer step, regardless of the high activity of the second step at a slope of 73 mV dec^{-1}. Table S7†

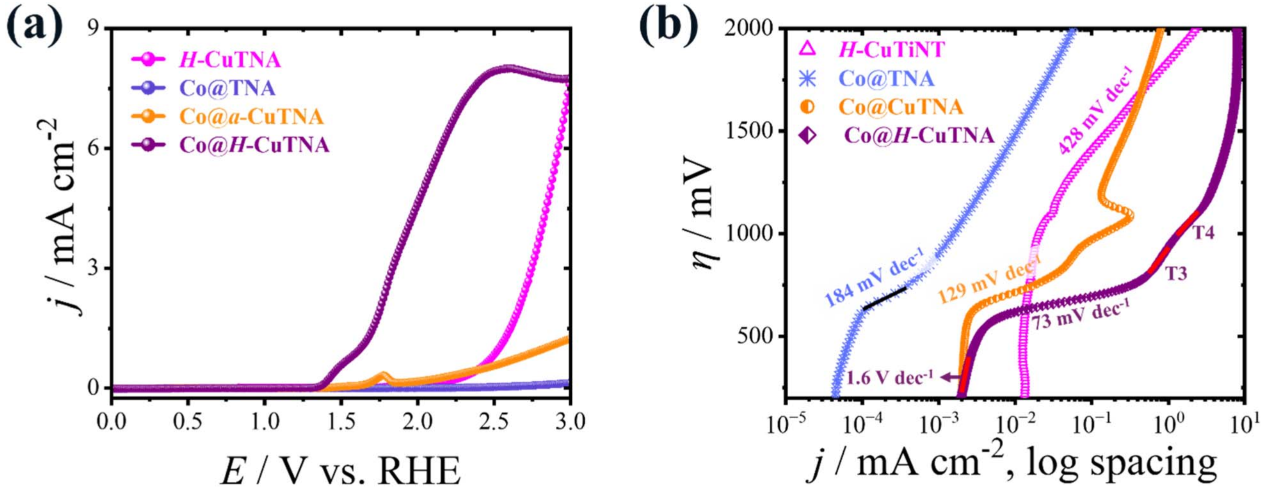

Fig. 6 (a) Steady state polarization curves of Co@CuTNA for 0.5 mM cobalt electrodeposited on p-TNA, a-CuTNA and H-CuTNA, compared to H-CuTNA treated at 500 °C recorded in 0.1 M glycerol +1 M KOH at a scan rate of 1 mV s^{-1}. (b) Corresponding Tafel plots for Co-electrodeposited samples.

summarizes the electrochemical parameters of Co-doped electrodes. Investigating the effects of Co deposition *via* cyclic voltammetry in Fig. S15(c)–(f)† shows that Co deposition does not affect the peak attributed to electron trappers as Co simply deposits on the surface without displacing Ti sites, especially for p-TNA electrodes. However, the a-CuTNA voltammogram gets constricted upon Co electrodeposition. To further investigate this phenomenon, we performed high resolution XPS analysis of Cu species for both air-annealed and hydrogen-treated samples. The addition of Co promotes Cu migration to the surface of the electrode due to the acidic precursor (4.4–5.4 pH) aiding in the leaching of Cu to the electrode surface, increasing the surface composition of Cu with increasing concentration of deposited Co, peaking at 1.06 at% of Cu (Table S9†) on the surface of the electrode for 50 mM Co@CuTNA. Additionally, for samples treated in 50 mM of Co precursor, peaks corresponding to hydroxyl Cu^{2+} (934.61 eV and 954.34 eV) doublets emerge as large amounts of Co oxidize the surface Cu sites, which reduces the efficacy of the electrode making it more susceptible to mass transfer limitations. The deconvoluted high-resolution XPS spectra in Fig. S21† of Co@H-CuTNA show the presence of both Co^{2+} (780.98 eV and 796.63 eV) and Co^{3+} (782.73 eV and 798.42 eV) doublets with prominent satellite features at 786.41 eV and 802.51 eV [Fig. S21†] which corresponds to CoO/Co_3O_4 species on the surface of the TNAs.

4. Conclusions

In summary, we have reported on significantly improving the conductivity and the electrocatalytic activity of anodic TiO_2 nanotubes by anodizing Ti–Cu alloy foils followed by treating the resultant electrodes in a controlled reducing environment. Despite the electronic limitations of TiO_2 nanotubes in electrochemical applications, we showed that through a simple decoration technique followed by a subsequent hydrogen treatment, the charge transfer resistance of TiO_2-based electrodes can be reduced by up to 16 times from pristine TNAs. The addition of Cu to TNAs showed improved kinetic performance as the Tafel slope decreases from 1255 mV dec^{-1} to 701 mV dec^{-1} for glycerol electro-oxidation, and decreases to 428 mV dec^{-1} when reduced at 500 °C. The observed increase in conductivity was attributed to Ti^{3+}/V_O defect formation, even in air-annealed Cu-decorated TNAs, showing a connection between Cu and point defects in the titania array. The amount of added Cu in the metal substrate was limited due to the formation of intermetallic sites that hinder anodic nanotube growth. However, the low loading of Cu at 3 at% in the substrate resulted in the distribution of Cu metal nanoparticles on the nanotube walls at diameters of 2–3 nm post-hydrogen treatment with optimum catalytic activity for CuTNAs. Additionally, Cu loading on titania nanotubes exhibited strong scaffold properties for co-catalyst deposition, facilitating charge transfer regardless of reduction in comparison to pristine TNAs. Albeit the conductivity limitations attributed to the electronic properties of titania, the Co-decorated reduced CuTNAs demonstrated a low onset potential of 1.37 V *vs.* RHE, and a Tafel slope of 73 mV dec^{-1}, as well as a Faradaic efficiency as high as 33.69% while selectively producing formic acid, an increase from the pristine TNA efficiency of 0.87%. By combining electronic modification of anatase titania with the synergistic electronic interactions between Cu and Co, we demonstrate a facile yet effective methodology to synthesize binder-free electrodes for the partial electrooxidation of glycerol with optimal selectivity towards key glycerol valorization products.

Data availability

The raw data supporting this article is available upon request from authors.

Author contributions

Ula Suliman: writing – original draft, methodology. Jing Liu: writing – review & editing, supervision, funding acquisition.

Shiva Mohajernia: writing – review & editing, supervision, funding acquisition.

Conflicts of interest

The authors declare that there are no conflicts of interest that could have influenced the work reported in this paper.

Acknowledgements

The authors acknowledge the Future Energy Systems Research, the Natural Sciences and Engineering Research Council of Canada (NSERC RGPIN-2024-06001), and Alberta Innovates (AH 232403375) for supporting this research. We would like to thank Dr Sadegh Pour-Ali, Dr Shiraz Merali and Taha Kubbar for their valuable assistance during the revision of this manuscript.

References

1 F. W. S. Lucas, R. G. Grim, S. A. Tacey, C. A. Downes, J. Hasse, A. M. Roman, C. A. Farberow, J. A. Schaidle and A. Holewinski, Electrochemical Routes for the Valorization of Biomass-Derived Feedstocks: From Chemistry to Application, *ACS Energy Lett.*, 2021, **6**, 1205–1270.

2 A. Dias da Silva Ruy, A. Luíza Freitas Ferreira, A. Ésio Bresciani R. Maria de Brito Alves and L. Antônio Magalhães Pontes, in *Biotechnological Applications of Biomass*, IntechOpen, 2021.

3 G. Dodekatos, S. Schünemann and H. Tüysüz, Recent Advances in Thermo-, Photo-, and Electrocatalytic Glycerol Oxidation, *ACS Catal.*, 2018, **8**, 6301–6333.

4 C. Tang, Y. Zheng, M. Jaroniec and S. Qiao, Electrocatalytic Refinery for Sustainable Production of Fuels and Chemicals, *Angew. Chem., Int. Ed.*, 2021, **60**, 19572–19590.

5 P. De Luna, C. Hahn, D. Higgins, S. A. Jaffer, T. F. Jaramillo and E. H. Sargent, What would it take for renewably powered electrosynthesis to displace petrochemical processes?, *Science*, 2019, **364**, eaav3506.

6 Y. Xu, M. Liu, S. Wang, K. Ren, M. Wang, Z. Wang, X. Li, L. Wang and H. Wang, Integrating electrocatalytic hydrogen generation with selective oxidation of glycerol to formate over bifunctional nitrogen-doped carbon coated nickel-molybdenum-nitrogen nanowire arrays, *Appl. Catal., B*, 2021, **298**, 120493.

7 M. H. Moklis, C. Shuo, S. Boonyubol and J. S. Cross, Electrochemical Valorization of Glycerol *via* Electrocatalytic Reduction into Biofuels: A Review, *ChemSusChem*, 2024, **17**, e202300990.

8 R. Li, K. Xiang, Z. Peng, Y. Zou and S. Wang, Recent Advances on Electrolysis for Simultaneous Generation of Valuable Chemicals at both Anode and Cathode, *Adv. Energy Mater.*, 2021, **11**, 2102292.

9 Y. X. Chen, A. Lavacchi, H. A. Miller, M. Bevilacqua, J. Filippi, M. Innocenti, A. Marchionni, W. Oberhauser, L. Wang and F. Vizza, Nanotechnology makes biomass electrolysis more energy efficient than water electrolysis, *Nat. Commun.*, 2014, **5**, 4036.

10 C. H. Lam, A. J. Bloomfield and P. T. Anastas, A switchable route to valuable commodity chemicals from glycerol *via* electrocatalytic oxidation with an earth abundant metal oxidation catalyst, *Green Chem.*, 2017, **19**, 1958–1968.

11 Y. Li, X. Wei, L. Chen, J. Shi and M. He, Nickel-molybdenum nitride nanoplate electrocatalysts for concurrent electrolytic hydrogen and formate productions, *Nat. Commun.*, 2019, **10**, 5335.

12 T. Hisatomi, J. Kubota and K. Domen, Recent advances in semiconductors for photocatalytic and photoelectrochemical water splitting, *Chem. Soc. Rev.*, 2014, **43**, 7520–7535.

13 K. E. Salem, A. M. Mokhtar, I. Soliman, M. Ramadan, B. S. Shaheen and N. K. Allam, Ge-doped ZnO nanorods grown on FTO for photoelectrochemical water splitting with exceptional photoconversion efficiency, *Int. J. Hydrogen Energy*, 2021, **46**, 209–220.

14 J. Zhang, Y. Shen and H. Li, Electrolysis of Glycerol by Non-Noble Metal Hydroxides and Oxides, *ACS Appl. Energy Mater.*, 2023, **6**, 5508–5518.

15 S. Mohajernia, S. Hejazi, A. Mazare, N. T. Nguyen and P. Schmuki, Photoelectrochemical H_2 Generation from Suboxide TiO_2 Nanotubes: Visible-Light Absorption *versus* Conductivity, *Chem.–Eur. J.*, 2017, **23**, 12406–12411.

16 P. Roy, S. Berger and P. Schmuki, TiO_2 Nanotubes: Synthesis and Applications, *Angew. Chem., Int. Ed.*, 2011, **50**, 2904–2939.

17 S. Hejazi, S. Pour-Ali, M. S. Killian and S. Mohajernia, One-dimensional suboxide TiO_2 nanotubes for electrodics applications, *Electrochem. Commun.*, 2022, **136**, 107246.

18 X. Hou, K. Aitola, H. Jiang, P. D. Lund and Y. Li, Reduced TiO_2 nanotube array as an excellent cathode for hydrogen evolution reaction in alkaline solution, *Catal. Today*, 2022, **402**, 3–9.

19 X. Zhou, N. Liu and P. Schmuki, Photocatalysis with TiO_2 Nanotubes: "Colorful" Reactivity and Designing Site-Specific Photocatalytic Centers into TiO_2 Nanotubes, *ACS Catal.*, 2017, **7**, 3210–3235.

20 H. Chen, N. Li, Y. H. Wu, J. Bin Shi, B. X. Lei and Z. F. Sun, A novel cheap, one-step and facile synthesis of hierarchical TiO_2 nanotubes as fast electron transport channels for highly efficient dye-sensitized solar cells, *Adv. Powder Technol.*, 2020, **31**, 1556–1563.

21 T. S. Rajaraman, S. P. Parikh and V. G. Gandhi, Black TiO_2: A review of its properties and conflicting trends, *Chem. Eng. J.*, 2020, **389**, 123918.

22 S. Mohajernia, S. Hejazi, A. Mazare, N. T. Nguyen, I. Hwang, S. Kment, G. Zoppellaro, O. Tomanec, R. Zboril and P. Schmuki, Semimetallic core-shell TiO_2 nanotubes as a high conductivity scaffold and use in efficient 3D-RuO_2 supercapacitors, *Mater. Today Energy*, 2017, **6**, 46–52.

23 E. Khorashadizade, S. Mohajernia, S. Hejazi, H. Mehdipour, N. Naseri, O. Moradlou, A. Z. Moshfegh and P. Schmuki, Intrinsically Ru-Doped Suboxide TiO_2 Nanotubes for Enhanced Photoelectrocatalytic H_2 Generation, *J. Phys. Chem. C*, 2021, **125**, 6116–6127.

24 U. Lačnjevac, R. Vasilić, A. Dobrota, S. Đurđić, O. Tomanec, R. Zbořil, S. Mohajernia, N. T. Nguyen, N. Skorodumova, D. Manojlović, N. Elezović, I. Pašti and P. Schmuki, High-performance hydrogen evolution electrocatalysis using proton-intercalated TiO_2 nanotube arrays as interactive supports for Ir nanoparticles, *J. Mater. Chem. A*, 2020, **8**, 22773–22790.

25 Ł. Haryński, K. Grochowska, J. Karczewski, J. Ryl, J. Rysz and K. Siuzdak, Free-standing TiO_2 nanotubes decorated with spherical nickel nanoparticles as a cost-efficient electrocatalyst for oxygen evolution reaction, *RSC Adv.*, 2020, **11**, 219–228.

26 B. Yan, D. Liu, X. Feng, M. Shao and Y. Zhang, Ru Species Supported on MOF-Derived N-Doped TiO_2/C Hybrids as Efficient Electrocatalytic/Photocatalytic Hydrogen Evolution Reaction Catalysts, *Adv. Funct. Mater.*, 2020, **30**, 2003007.

27 N. S. Peighambardoust, S. Khameneh Asl, R. Mohammadpour and S. K. Asl, Band-gap narrowing and electrochemical properties in N-doped and reduced anodic TiO_2 nanotube arrays, *Electrochim. Acta*, 2018, **270**, 245–255.

28 M. Kim, J. Choi, W. Lee, Y.-Y. Ahn, H. Lee, K. Cho and J. Lee, Performance of Magnéli phase Ti_4O_7 and Ti^{3+} self-doped TiO_2 as oxygen vacancy-rich titanium oxide anodes: comparison in terms of treatment efficiency, anodic degradative pathways, and long-term stability, *Appl. Catal., B*, 2023, **337**, 122993.

29 P. Si, M. Li, X. Wang, F. Sun, J. Liu, Q. Wang, F. Ren, H. Kong and Y. Wang, Origin of Enhanced Electricity Generation on Magnéli Phase Titanium Suboxide Nanocrystal Films, *ACS Appl. Energy Mater.*, 2021, **4**, 10877–10885.

30 P. Paunović, O. Popovski, E. Fidanevska, B. Ranguelov, D. Stoevska Gogovska, A. T. Dimitrov and S. Hadi Jordanov, Co-Magneli phases electrocatalysts for hydrogen/oxygen evolution, *Int. J. Hydrogen Energy*, 2010, **35**, 10073–10080.

31 J. R. Smith, F. C. Walsh and R. L. Clarke, Electrodes based on Magnéli phase titanium oxides: the properties and applications of Ebonex® materials, *J. Appl. Electrochem.*, 1998, **28**, 1021–1033.

32 B. M. Jović, U. Lačnjevac, V. D. Jović, L. J. Gajić-Krstajić, J. Kovač, D. Poleti and N. V. Krstajić, Ni-(Ebonex-supported Ir) composite coatings as electrocatalysts for alkaline water electrolysis. Part II: oxygen evolution, *Int. J. Hydrogen Energy*, 2016, **41**, 20502–20514.

33 S. Mohajernia, P. Andryskova, G. Zoppellaro, S. Hejazi, S. Kment, R. Zboril, J. Schmidt and P. Schmuki, Influence of Ti^{3+} defect-type on heterogeneous photocatalytic H_2 evolution activity of TiO_2, *J. Mater. Chem. A*, 2020, **8**, 1432–1442.

34 S. Mohajernia, S. Hejazi, A. Mazare, N. T. Nguyen and P. Schmuki, Photoelectrochemical H_2 Generation from Suboxide TiO_2 Nanotubes: Visible-Light Absorption *versus* Conductivity, *Chem.–Eur. J.*, 2017, **23**, 12406–12411.

35 A. Naldoni, M. Altomare, G. Zoppellaro, N. Liu, Š. Kment, R. Zbořil and P. Schmuki, Photocatalysis with Reduced TiO_2 : From Black TiO_2 to Cocatalyst-Free Hydrogen Production, *ACS Catal.*, 2019, **9**, 345–364.

36 G. Martra, Lewis acid and base sites at the surface of microcrystalline TiO_2 anatase: relationships between surface morphology and chemical behaviour, *Appl. Catal., A*, 2000, **200**, 275–285.

37 H. Yan, B. Liu, X. Zhou, F. Meng, M. Zhao, Y. Pan, J. Li, Y. Wu, H. Zhao, Y. Liu, X. Chen, L. Li, X. Feng, D. Chen, H. Shan, C. Yang and N. Yan, Enhancing polyol/sugar cascade oxidation to formic acid with defect rich MnO_2 catalysts, *Nat. Commun.*, 2023, (14), 1–11.

38 L. Wu, Q. Wu, Y. Han, D. Zhang, R. Zhang, N. Song, X. Wu, J. Zeng, P. Yuan, J. Chen, A. Du, K. K. Huang and X. Yao, Strengthening the Synergy between Oxygen Vacancies in Electrocatalysts for Efficient Glycerol Electrooxidation, *Adv. Mater.*, 2024, **36**, 2401857.

39 S. Hejazi, M. Altomare, N. T. Nguyen, S. Mohajernia, M. Licklederer and P. Schmuki, Intrinsic Au-decoration on anodic TiO_2 nanotubes grown from metastable Ti–Au sputtered alloys—High density co-catalyst decoration enhances the photocatalytic H_2 evolution, *Appl. Mater. Today*, 2019, **14**, 118–125.

40 B. E. Sanabria-Arenas, A. Mazare, J. Yoo, N. T. Nguyen, S. Hejazi, H. Bian, M. V. Diamanti, M. P. Pedeferri and P. Schmuki, Intrinsic AuPt-alloy particles decorated on TiO2 nanotubes provide enhanced photocatalytic degradation, *Electrochim. Acta*, 2018, **292**, 865–870.

41 H. Bian, N. T. Nguyen, J. Yoo, S. Hejazi, S. Mohajernia, J. Müller, E. Spiecker, H. Tsuchiya, O. Tomanec, B. E. Sanabria-Arenas, R. Zboril, Y. Y. Li and P. Schmuki, Forming a Highly Active, Homogeneously Alloyed AuPt Co-catalyst Decoration on TiO_2 Nanotubes Directly During Anodic Growth, *ACS Appl. Mater. Interfaces*, 2018, **10**, 18220–18226.

42 M. Sheikhzadeh, S. Hejazi, S. Mohajernia, O. Tomanec, M. Mokhtar, A. Alshehri, S. Sanjabi, R. Zboril and P. Schmuki, Photocatalytic H_2 Evolution: Dealloying as Efficient Tool for the Fabrication of Rh-decorated TiO_2 Nanotubes, *ChemCatChem*, 2019, **11**, 6258–6262.

43 D. R. Santos, C. R. Martins and C. de Arruda Rodrigues, Characterization of nanotubular oxide layer grown on Ti14wt.%Nb alloy by anodization and its performance in photoelectrocatalytic process, *J. Solid State Electrochem.*, 2020, **24**, 1877–1888.

44 S. Hejazi, S. Mohajernia, Y. Wu, P. Andryskova, G. Zoppellaro, I. Hwang, O. Tomanec, R. Zboril and P. Schmuki, Intrinsic Cu nanoparticle decoration of TiO_2 nanotubes: a platform for efficient noble metal free photocatalytic H_2 production, *Electrochem. Commun.*, 2019, **98**, 82–86.

45 W. Chen, J. Xu, F. Huang, C. Zhao, Y. Guan, Y. Fang, J. Hu, W. Yang, Z. Luo and Y. Guo, CO oxidation over CuO_x/TiO_2 catalyst: the importance of oxygen vacancies and Cu^+ species, *Appl. Surf. Sci.*, 2023, **618**, 156539.

46 Y. Wang, S. Deng, B. Liu and Y. Jin, Mechanistic Understanding on the Role of Cu Species over the CuO_x/TiO_2 Catalyst for CO_2 Photoreduction, *ACS Omega*, 2020, **5**, 18050–18063.

47 G. Li, N. M. Dimitrijevic, L. Chen, T. Rajh and K. A. Gray, Role of Surface/Interfacial Cu^{2+} Sites in the Photocatalytic Activity of Coupled CuO–TiO_2 Nanocomposites, *J. Phys. Chem. C*, 2008, **112**, 19040–19044.

48 J. A. Torres, J. C. da Cruz, A. E. Nogueira, G. T. S. T. da Silva, J. A. de Oliveira and C. Ribeiro, Role of CuO–TiO_2 interaction in catalyst stability in CO_2 photoreduction process, *J. Environ. Chem. Eng.*, 2022, **10**, 107291.

49 V. Polliotto, S. Livraghi, A. Krukowska, M. V. Dozzi, A. Zaleska-Medynska, E. Selli and E. Giamello, Copper-Modified TiO_2 and $ZrTiO_4$: Cu Oxidation State Evolution during Photocatalytic Hydrogen Production, *ACS Appl. Mater. Interfaces*, 2018, **10**, 27745–27756.

50 L. Liu, F. Gao, H. Zhao and Y. Li, Tailoring Cu valence and oxygen vacancy in Cu/TiO_2 catalysts for enhanced CO_2 photoreduction efficiency, *Appl. Catal., B*, 2013, **134–135**, 349–358.

51 C. Liu, M. Hirohara, T. Maekawa, R. Chang, T. Hayashi and C. Y. Chiang, Selective electro-oxidation of glycerol to dihydroxyacetone by a non-precious electrocatalyst – CuO, *Appl. Catal., B*, 2020, **265**, 118543.

52 M. E. Ghaith, M. G. Abd El-Moghny, G. A. El-Nagar, H. H. Alalawy, M. E. El-Shakre and M. S. El-Deab, Tailor-designed binary Ni–Cu nano dendrites decorated 3D-carbon felts for efficient glycerol electrooxidation, *RSC Adv.*, 2023, **13**, 895–905.

53 G. A. El-Nagar, I. Derr, T. Kottakkat and C. Roth, Auspicious Metal-Doped-Cu_2O/Cu Dendrite (M=Ni, Co, Fe) Catalysts for Direct Alkaline Fuel Cells: Effect of Dopants, *ECS Trans.*, 2017, **80**, 1013–1022.

54 B. Kumari, M. Braun, S. Cychy, I. Sanjuán, G. Behrendt, M. Behrens, M. Muhler and C. Andronescu, Electrooxidation of the Glycerol Derivative Solketal over Cu–Co Hydroxycarbonates to Enable the Synthesis of Glyceric Acid, *ChemElectroChem*, 2023, **10**, e202300018.

55 K. Kawashima, R. A. Márquez, Y. J. Son, C. Guo, R. R. Vaidyula, L. A. Smith, C. E. Chukwuneke and C. B. Mullins, Accurate Potentials of Hg/HgO Electrodes: Practical Parameters for Reporting Alkaline Water Electrolysis Overpotentials, *ACS Catal.*, 2023, **13**, 1893–1898.

56 M. H. Mueller and H. W. Knott, The Crystal Structures of Ti_2Cu, Ti_2Ni, Ti_4Ni_2O, and Ti_4Cu_2O, *Transactions of American Institute of Metallurgical Engineers*, 1963, 227.

57 Á. Balog, G. F. Samu, S. Petö and C. Janáky, The Mystery of Black TiO_2: Insights from Combined Surface Science and *in situ* Electrochemical Methods, *ACS Mater. Au*, 2021, **1**, 157–168.

58 N. K. Shrestha and P. Schmuki, in *Electrochemistry*, Royal Society of Chemistry, 2013, vol. 12, pp. 87–131.

59 E. Yelekli Kirici, S. Angizi and D. Higgins, A Universal Roadmap for Quantification of Glycerol Electrooxidation Products Using Proton Nuclear Magnetic Spectroscopy (1H NMR), *ACS Catal.*, 2024, **14**, 9328–9341.

60 H. Zhou and Y. Zhang, Electrochemically self-doped TiO_2 nanotube arrays for supercapacitors, *J. Phys. Chem. C*, 2014, **118**, 5626–5636.

61 F. Fabregat-Santiago, E. M. Barea, J. Bisquert, G. K. Mor, K. Shankar and C. A. Grimes, High carrier density and capacitance in TiO_2 nanotube arrays induced by electrochemical doping, *J. Am. Chem. Soc.*, 2008, **130**, 11312–11316.

62 C. C. L. McCrory, S. Jung, I. M. Ferrer, S. M. Chatman, J. C. Peters and T. F. Jaramillo, Benchmarking Hydrogen Evolving Reaction and Oxygen Evolving Reaction Electrocatalysts for Solar Water Splitting Devices, *J. Am. Chem. Soc.*, 2015, **137**, 4347–4357.

63 P. Cördoba-Torres, T. J. Mesquita and R. P. Nogueira, Relationship between the origin of constant-phase element behavior in electrochemical impedance spectroscopy and electrode surface structure, *J. Phys. Chem. C*, 2015, **119**, 4136–4147.

64 S. A. Ali Yahia, L. Hamadou, A. Kadri, N. Benbrahim and E. M. M. Sutter, Effect of Anodizing Potential on the Formation and EIS Characteristics of TiO_2 Nanotube Arrays, *J. Electrochem. Soc.*, 2012, **159**, K83–K92.

65 M. Schalenbach, Y. E. Durmus, H. Tempel, H. Kungl and R. A. Eichel, Double layer capacitances analysed with impedance spectroscopy and cyclic voltammetry: validity and limits of the constant phase element parameterization, *Phys. Chem. Chem. Phys.*, 2021, **23**, 21097–21105.

66 O. Gharbi, M. T. T. Tran, B. Tribollet, M. Turmine and V. Vivier, Revisiting cyclic voltammetry and electrochemical impedance spectroscopy analysis for capacitance measurements, *Electrochim. Acta*, 2020, **343**, 136109.

67 K. Gelderman, L. Lee and S. W. Donne, Flat-band potential of a semiconductor: using the Mott–Schottky equation, *J. Chem. Educ.*, 2007, **84**, 685–688.

68 B. Bera, A. Chakraborty, T. Kar, P. Leuaa and M. Neergat, Density of States, Carrier Concentration, and Flat Band Potential Derived from Electrochemical Impedance Measurements of N-Doped Carbon and Their Influence on Electrocatalysis of Oxygen Reduction Reaction, *J. Phys. Chem. C*, 2017, **121**, 20850–20856.

69 C. Anastasescu, N. Spataru, D. Culita, I. Atkinson, T. Spataru, V. Bratan, C. Munteanu, M. Anastasescu, C. Negrila and I. Balint, Chemically assembled light harvesting CuO_x–TiO_2 p–n heterostructures, *Chem. Eng. J.*, 2015, **281**, 303–311.

70 Z. Niu, S. Fan, X. Li, Z. Liu, J. Wang, J. Duan, M. O. Tadé and S. Liu, Facile Tailoring of the Electronic Structure and the d-Band Center of Copper-Doped Cobaltate for Efficient Nitrate Electrochemical Hydrogenation, *ACS Appl. Mater. Interfaces*, 2022, **14**, 35477–35484.